

Article

On the Influence of Direction-Dependent Behavior of Rock Mass in Simulations of Deep Tunneling Using a Novel Gradient-Enhanced Transversely Isotropic Damage–Plasticity Model

Thomas Mader * , Magdalena Schreter  and Günter Hofstetter 

Unit of Strength of Materials and Structural Analysis, Department of Basic Sciences in Engineering Sciences, University of Innsbruck, Technikerstraße 13, A-6020 Innsbruck, Austria

* Correspondence: thomas.mader@uibk.ac.at

Abstract: In engineering practice, numerical simulations of deep tunneling are commonly based on isotropic linear–elastic perfectly plastic rock models. Rock, however, commonly exhibits highly nonlinear and distinct direction-dependent mechanical behavior. The former is characterized by irreversible deformation, associated with strain hardening and strain softening, and the degradation of stiffness; the latter is due to the inherent rock structure. Nevertheless, the majority of the existing rock models focuses on the prediction of either the highly nonlinear material behavior or the inherent anisotropic response of rock. The combined effects of nonlinear and direction-dependent rock behavior, particularly in the context of the numerical simulations of tunnel excavation, have rarely been taken into account so far. Thus, it is the aim of the present contribution to demonstrate the influence of both effects on the evolution of the deformation and stress distribution in the rock mass due to deep tunnel excavation on the example of a well-monitored stretch of the Brenner Base Tunnel (BBT). To this end, the recently proposed gradient-enhanced transversely isotropic rock damage–plasticity (TI-RDP) model, is employed for modeling the surrounding rock mass consisting of Innsbruck quartz–phyllite. The material parameters for the nonlinear transversely isotropic rock model are identified by means of three-dimensional finite element simulations of triaxial tests on specimens of Innsbruck quartz–phyllite, conducted for varying loading angles with respect to the foliation planes and different confining pressures. Subsequently, the results of the nonlinear 2D finite element simulations of tunnel excavation are presented for different anisotropy parameters and different orientations of the principal material directions with respect to the tunnel axis. The capabilities of the TI-RDP model are assessed by comparing the numerically predicted results with those obtained by the isotropic version of the RDP model.



Citation: Mader, T.; Schreter, M.; Hofstetter, G. On the Influence of Direction-Dependent Behavior of Rock Mass in Simulations of Deep Tunneling Using a Novel Gradient-Enhanced Transversely Isotropic Damage–Plasticity Model. *Appl. Sci.* **2022**, *12*, 8532. <https://doi.org/10.3390/app12178532>

Academic Editors: Sabrina Bonetto, Pietro Mosca and Chiara Caselle

Received: 19 July 2022

Accepted: 22 August 2022

Published: 26 August 2022

Publisher's Note: MDPI stays neutral with regard to jurisdictional claims in published maps and institutional affiliations.



Copyright: © 2022 by the authors. Licensee MDPI, Basel, Switzerland. This article is an open access article distributed under the terms and conditions of the Creative Commons Attribution (CC BY) license (<https://creativecommons.org/licenses/by/4.0/>).

Keywords: rock mechanics and rock engineering for infrastructures; rock properties; anisotropy; transverse isotropy; tunneling

1. Introduction

In numerical simulations of tunnel advance, the constitutive model for the surrounding rock mass is a key component for obtaining realistic deformations and stress states. However, in most of the existing tunneling simulations considered in a practical engineering context, frequently isotropic linear–elastic perfectly plastic material models are employed, neglecting two essential characteristics of the mechanical behavior of rock: First, the mechanical behavior of rock is highly nonlinear. This is manifested by a nonlinear response in triaxial compression, irreversible deformation including strain hardening in the pre-peak regime as well as strain softening, accompanied by a degradation of the material stiffness, in the post-peak regime of the stress–strain relations. Second, depending

on the genesis of a particular rock, inherent structures, such as stratification or foliation planes, lead to a distinct inherent anisotropic material behavior.

Typical approaches for capturing the nonlinear and potentially anisotropic mechanical behavior of rock mass can be classified into two main categories: (i) continuum-based approaches, treating rock mass as an equivalent continuum with smeared properties of both rock and discontinuities, and (ii) discontinuum approaches, in which discontinuities between pieces of intact rock are modeled in a discrete manner. The scope of this publication is on the continuum-based modeling of rock; readers interested in discontinuum modeling are referred to the literature, e.g., Lisjak and Grasselli [1], Jing and Hudson [2], Jing [3], Barton [4] or Wittke [5].

In contrast to discontinuum approaches, continuum-based approaches offer an approximate but computationally more efficient approach for modeling rock mass, as inherent discontinuities and intact rock are modeled in a smeared manner as a quasi-continuum. For estimating the mechanical properties, either a homogenization procedure based on a representative volume element, or, as an alternative, empirical relations may be employed. A popular representative of the last category was proposed by Hoek et al. [6,7] for estimating the strength and stiffness of quasi-homogeneous rock mass based on a rock mass classification system.

Continuum-based modeling approaches assuming quasi-isotropic elasto-plastic behavior have been widely used since the 1970s. Most of them use failure criteria according to Hoek–Brown [8] or Mohr–Coulomb. For a realistic modeling of the highly nonlinear mechanical behavior of rock, Unteregger et al. [9] proposed an isotropic rock damage–plasticity model. It originates from the well-established concrete model by Grassl and Jirásek [10] and incorporates linear elasticity, hardening plasticity with non-associated plastic flow as well as strain softening resulting from damage due to micro-cracking. The smooth Hoek–Brown failure criterion, proposed by Menétrey and Willam [11] is used as an ultimate strength envelope. For objectively capturing structural failure mechanisms, such as the formation of shear bands in the context of tunnel excavation or borehole breakout, the model was extended by an over-nonlocal implicit gradient-enhanced formulation by Schreter et al. [12].

The above mentioned models are restricted to rock types with isotropic material behavior. However, inherent anisotropy associated with an oriented microstructure of rock may have a significant impact on predicting the mechanical behavior. Especially in a stratified or foliated rock mass, e.g., shales or phyllites, often the special cases of orthotropic or transversely isotropic material behavior arise.

For considering such inherent direction dependence in continuum-based models, several approaches have been developed in the past: anisotropic yield functions were proposed by Hill [13], Pariseau [14] and Tsai and Wu [15], amongst others. Ubiquitous joint models, building upon the *single plane of weakness theory* by Jaeger [16], in which failure—in the rock matrix, along oriented joints or in both—may occur, were proposed by Goodman et al. [17] and Ismael et al. [18,19]. An anisotropic generalization of isotropic failure criteria by means of scalar anisotropy parameters was proposed by Pietruszczak and Mroz [20], Gao et al. [21], Chen et al. [22,23] and Parisio et al. [24]. Alternatively, by means of a linear mapping of the Cauchy stress tensor into a fictitious isotropic configuration, originally proposed by Boehler [25], a transversely isotropic failure criterion was obtained as an extension of an isotropic failure criterion. This approach was applied in several works, e.g., [26–31]. The last three mentioned concepts, i.e., ubiquitous joint models, generalization of isotropic failure criteria by means of scalar anisotropy parameters and linear mapping into a fictitious isotropic configuration, were part of a comprehensive review for considering transversely isotropic material behavior by Mader et al. [32]. The mapping of the Cauchy stress tensor into a fictitious isotropic configuration turned out to be the most versatile modeling approach. Thus, the transversely isotropic rock damage–plasticity (TI-RDP) model was proposed by combining the isotropic rock damage–plasticity model [9,12] and the approach by Boehler [25]. Based on three-dimensional (3D) FE simulations of triaxial compression tests, it was shown that the TI-RDP model is well suited for modeling

the inherent direction-dependent and highly nonlinear behavior of stratified or foliated rock types in a realistic manner.

Modeling the tunnel excavation or borehole breakout was subject of numerous publications, e.g., [27,33–38]. In Schreter et al. [39], the importance of employing advanced constitutive models for rock mass and shotcrete for predicting the mechanical behavior of deep tunnels was demonstrated. In Wang et al. [40], numerical simulations of the failure mechanism of tunneling in transversely isotropic rock mass were presented. Schuller and Schweiger [41] investigated the deformation behavior of a tunnel structure using a multi-laminate model for the surrounding rock mass, considering directional dependencies but not damaging processes. Pardoen et al. [42] investigated the influence of transversely isotropic elasto-plastic material behavior on the evolution of shear bands during tunnel excavation, considering the approach by Pietruszczak and Mroz [20] and including strain hardening and softening. For regularizing the softening behavior, a local second gradient model was used.

The combined effect of the highly nonlinear material behavior and the inherent anisotropic response of rock is inevitable in particular for the numerical analysis of potential collapse of a tunnel structure in stratified or foliated rock mass.

Thus, in this contribution the influence of both the highly nonlinear and anisotropic mechanical behavior of stratified or foliated rock mass on the deformation, stress distribution and stability during tunnel excavation, will be systematically investigated on the example of a well-monitored stretch of the Brenner Base Tunnel (BBT), which connects Austria and Italy through the Eastern Alps (cf. Figure 1). For a more detailed representation of the geology, interested readers are referred to, for example, Foderà et al. [43] or Bistacchi et al. [44].

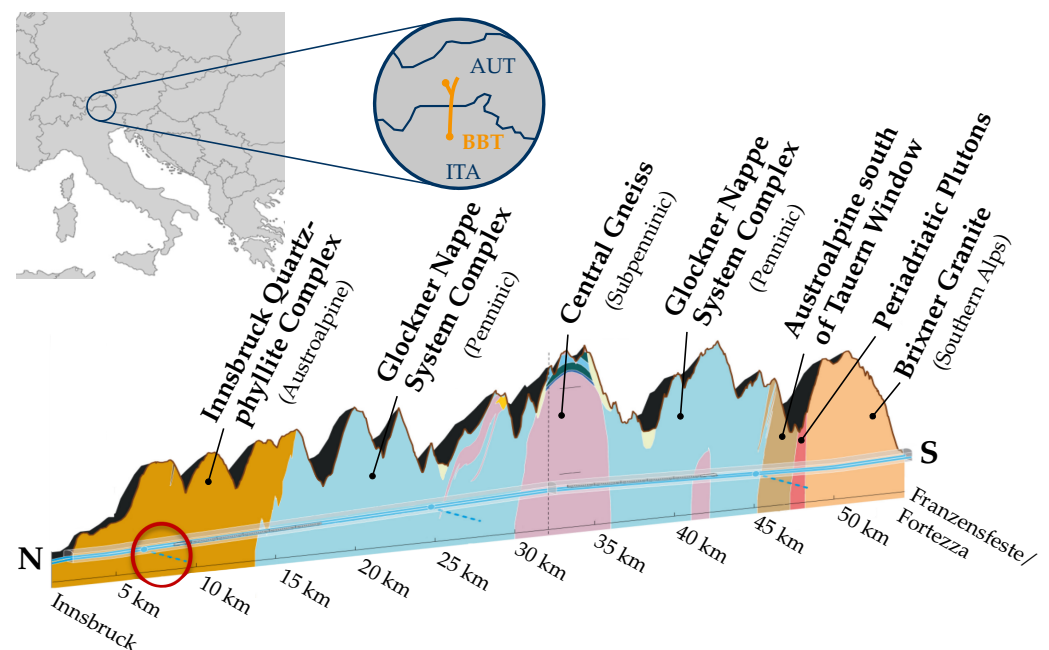


Figure 1. Geology of the Brenner Base Tunnel (BBT) from Innsbruck (left) to Franzensfeste/Forzezza (right) and location (red circle) of the considered stretch (adapted with permission from Ref. [45], 2019, BBT SE).

To this end, the recently proposed continuum-based rock model will be enhanced for considering the influence of discontinuities, i.e., joints and faults, in rock mass. The latter are considered by reducing the intact rock parameters independent of the orientation of the discontinuities in terms of the geological strength index GSI, whereas the anisotropic mechanical behavior only refers to the stratification or foliation planes of intact rock. The material parameters will be identified by means of 3D finite element simulations of triaxial tests on specimens of quartz-phyllite belonging to the Innsbruck quartz-phyllite

complex according to Figure 1. They were conducted for varying loading angles with respect to the foliation planes and different confining pressures.

The remainder of the paper is organized as follows: In Section 2, the equations of the TI-RDP model are briefly summarized and extended for modeling stratified or foliated rock mass (in contrast to intact rock). In Section 3, the calibration of the material parameters by means of 3D finite element simulations of triaxial tests on *Innsbruck quartz-phyllite* with different loading directions with respect to the foliation planes and different confining pressures are presented. In Section 4, the influence of the orientation of foliation planes on the mechanical behavior of the rock mass during tunnel excavation is assessed by means of 2D finite element simulations, and a comparison with the results from a related study by Schreter et al. [12], using an *isotropic* rock damage–plasticity model, is presented. Finally, in Section 5, the paper is closed with a summary and a discussion on recommended future research activities.

2. A Transversely Isotropic Damage–Plasticity Model for Intact Rock and Rock Mass

In the following, the transversely isotropic damage–plasticity (TI-RDP) model, proposed by Mader et al. [32], is described briefly and extended for considering the mechanical behavior of rock mass. A description of the used symbols is provided in Table A1 in Appendix A. The TI-RDP model is based on a combination of the isotropic damage–plasticity model, proposed by Unteregger et al. [9], extended by an implicit gradient-enhanced regularization scheme in Schreter et al. [12], and the approach by Boehler [25] for capturing transversely isotropic material behavior.

Based on the theories of plasticity and damage mechanics, the stress–strain relation of the TI-RDP model, defined in the global coordinate system, reads as

$$\sigma = (1 - \omega) \mathbb{C}^{(ti)} : (\varepsilon - \varepsilon^{(p)}) \tag{1}$$

where σ denotes the nominal Cauchy stress tensor (force per total area), ω is the scalar isotropic damage variable ranging from 0 (undamaged material) to 1 (completely damaged material), ε and $\varepsilon^{(p)}$ represent the total and the plastic strain tensor, respectively. The fourth-order transversely isotropic elastic stiffness tensor with respect to the global coordinate system

$$\mathbb{C}_{ijkl}^{(ti)} = a_{mi} a_{nj} a_{pk} a_{ql} \mathbb{C}'_{mnpq} \tag{2}$$

is obtained by transforming the transversely isotropic elastic stiffness tensor $\mathbb{C}'^{(ti)}$, aligned with the principal directions of the material, into the global coordinate system by means of the orthogonal transformation matrix \mathbf{a} . In Voigt notation, $\mathbb{C}'^{(ti)}$ reads as

$$\mathbb{C}'^{(ti)} = r_s \begin{bmatrix} \frac{1}{E_1} & -\frac{\nu_{12}}{E_2} & -\frac{\nu_{12}}{E_2} & 0 & 0 & 0 \\ -\frac{\nu_{12}}{E_2} & \frac{1}{E_2} & -\frac{\nu_{23}}{E_2} & 0 & 0 & 0 \\ -\frac{\nu_{12}}{E_2} & -\frac{\nu_{23}}{E_2} & \frac{1}{E_2} & 0 & 0 & 0 \\ 0 & 0 & 0 & \frac{1}{G_{12}} & 0 & 0 \\ 0 & 0 & 0 & 0 & \frac{1}{G_{12}} & 0 \\ 0 & 0 & 0 & 0 & 0 & \frac{2(1+\nu_{23})}{E_2} \end{bmatrix}^{-1} \tag{3}$$

characterized by five independent material parameters, i.e., the Young’s modulus E_1 in the direction of the normal vector \mathbf{n} to the planes of isotropy (planes with the same material parameters in all directions within those planes), i.e., \mathbf{n} represents the axis of material symmetry, as illustrated in Figure 2, the Poisson’s ratio ν_{12} and the shear modulus G_{12} in the planes containing the axis of material symmetry, and the Young’s modulus E_2 as well as the Poisson’s ratio ν_{23} , both in the plane of isotropic material behavior.

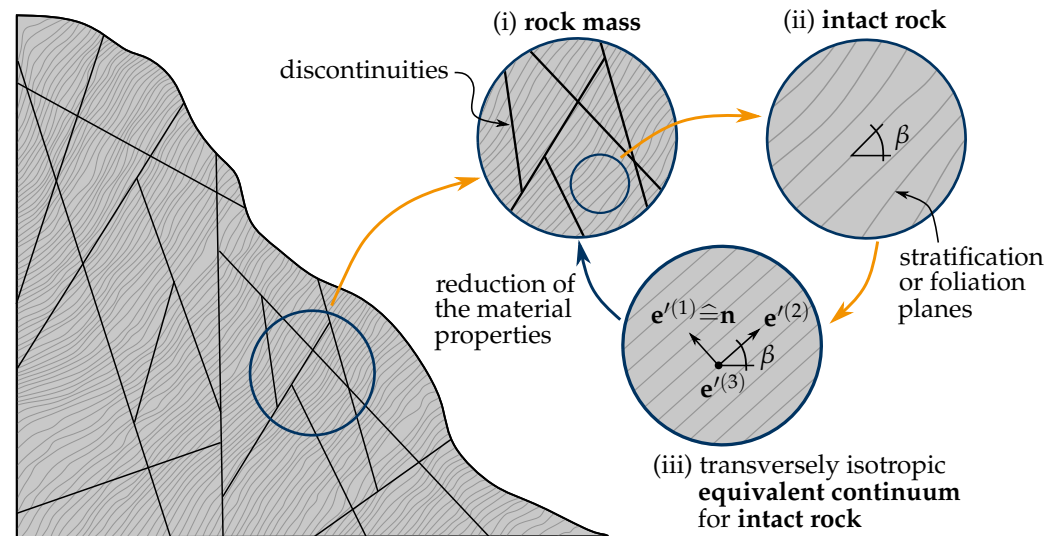


Figure 2. Schematic sketch of (i) the discontinuities in rock mass, (ii) the stratification or foliation planes in intact rock and its consideration in the TI-RDP model by (iii) the transversely isotropic equivalent continuum for stratified or foliated intact rock.

As shown in Figure 2, in contrast to intact rock, which is characterized by a stratification or a pervasive foliation, the macro structure of rock mass is governed by mechanical discontinuities, such as joints and faults, resulting in a strong dependence of the material properties of rock mass on the surface conditions of those discontinuities. Thus, by analogy to the isotropic version of the RDP model, the elastic stiffness properties of intact rock, i.e., the Young’s moduli E_1 and E_2 as well as the shear modulus G_{12} are multiplied by the empirical stiffness reduction factor

$$r_s = 0.02 + \frac{1 - D/2}{1 + \exp\left(\frac{60 + 15 \cdot D - \text{GSI}}{11}\right)} + \left(0.98 - \frac{1}{1 + \exp(-40/11)}\right) \left(\frac{\text{GSI}}{100}\right)^{10} \quad (4)$$

according to Hoek et al. [6]. The latter is expressed in terms of the geological strength index (GSI) for considering the geological conditions of rock mass, ranging from 1 (intact rock) to 0 (completely disintegrated rock), and the disturbance factor D for taking into account the disturbance of the in situ stress in the rock mass due to the excavation process with 0 (undisturbed) $\leq D \leq 1$ (significantly disturbed). According to Hoek et al. [7], for excellent quality controlled blasting or mechanized tunneling, $D = 0$ is recommended.

2.1. Transversely Isotropic Plasticity Formulation

The plastic part of the TI-RDP model is formulated in terms of the effective stress tensor $\bar{\sigma}$ (force per undamaged area), which is linked to the nominal stress tensor σ by $\bar{\sigma} = \sigma / (1 - \omega)$. For considering the transversely isotropic behavior, a fictitious effective stress tensor

$$\bar{\sigma}^* = \mathbb{P} : \bar{\sigma} \quad (5)$$

is defined by mapping the effective stress tensor into a fictitious isotropic configuration, denoted by the superscript $(\bullet)^*$, as originally proposed by Boehler [25] and for instance applied by Semnani et al. [28], Borja et al. [46] and Bryant [29,47]. \mathbb{P} denotes the fourth-order linear mapping tensor with major and minor symmetry, reading in terms of the Walpole algebra [48] as

$$\mathbb{P} = \mathbb{E}^{(1)} + \gamma \left(\mathbb{E}^{(2)} + \mathbb{F} + \delta \mathbb{G} \right) \quad (6)$$

with the anisotropy parameters γ and δ . The latter are linked to the uniaxial compressive strength for intact rock perpendicular to the planes of isotropy $f_{cu}^{(1)}$, the uniaxial compressive

strength parallel to the latter $f_{cu}^{(2)}$, the shear strength in planes perpendicular to the planes of isotropy $f_{sh}^{(12)}$ and the shear strength in the plane of isotropy $f_{sh}^{(23)}$ by

$$\gamma = \frac{f_{cu}^{(1)}}{f_{cu}^{(2)}} \quad \text{and} \quad \delta = \frac{f_{sh}^{(23)}}{f_{sh}^{(12)}}. \tag{7}$$

γ can be determined by means of uniaxial compression tests with loading directions perpendicular and parallel to the planes of isotropy of intact layered rock. δ can be determined by simple shear tests with loading in planes perpendicular to the planes of isotropy and in the plane of isotropy of intact layered rock. According to (7), γ and δ are limited to values greater than 0 for a meaningful physical interpretation. The sub-tensors

$$\begin{aligned} \mathbb{E}_{ijkl}^{(1)} &= \phi_{ij}\phi_{kl}, \quad \mathbb{E}_{ijkl}^{(2)} = \frac{1}{2} \chi_{ij} \chi_{kl}, \quad \mathbb{F}_{ijkl} = \frac{1}{2} (\chi_{ik} \chi_{jl} + \chi_{il} \chi_{jk} - \chi_{ij} \chi_{kl}), \\ \mathbb{G}_{ijkl} &= \frac{1}{2} (\phi_{ik} \chi_{jl} + \phi_{il} \chi_{jk} + \chi_{ik} \phi_{jl} + \chi_{il} \phi_{jk}) \end{aligned} \tag{8}$$

describe the influence of the stratification or foliation planes on the material behavior, based on the microstructure tensor $\phi = \mathbf{n} \otimes \mathbf{n}$ and its orthogonal tensor $\chi = \mathbf{1} - \phi$, which are both defined by the normal vector \mathbf{n} of the planes of isotropy.

For delimiting the elastic domain, a direction-dependent yield criterion is formulated by expressing the yield function of the original isotropic RDP model in terms of the Haigh–Westergaard coordinates $\bar{\sigma}_m^*$, $\bar{\rho}^*$ and $\bar{\theta}^*$ of the mapped effective stress tensor $\bar{\sigma}^*$:

$$\begin{aligned} f^*(\bar{\sigma}^*, q_h(\alpha_p)) &= \left(\frac{1 - q_h(\alpha_p)}{f_{cu}^{(1)2}} \left(\bar{\sigma}_m^* + \frac{\bar{\rho}^*}{\sqrt{6}} \right)^2 + \sqrt{\frac{3}{2}} \frac{\bar{\rho}^*}{f_{cu}^{(1)}} \right)^2 \\ &\quad + \frac{q_h^2(\alpha_p)}{f_{cu}^{(1)}} r_m \cdot m_0^* \left(\bar{\sigma}_m^* + r(\bar{\theta}^*, e) \frac{\bar{\rho}^*}{\sqrt{6}} \right) - r_c \cdot q_h^2(\alpha_p). \end{aligned} \tag{9}$$

According to (5), the mapped effective stress depends on the mapping tensor \mathbb{P} and thus incorporates the orientation of the principal material directions and the anisotropy parameters. The parameters of the yield function comprise the uniaxial compressive strength for loading perpendicular to the planes of isotropy $f_{cu}^{(1)}$, the friction parameter for intact rock m_0^* and two empirical reduction factors, r_m and r_c , for considering the influence of discontinuities on the friction and cohesion in rock mass by analogy to the original isotropic RDP model. Hoek et al. [7] proposed the latter as

$$r_m = \exp\left(\frac{\text{GSI} - 100}{28 - 14D}\right) \tag{10}$$

and

$$r_c = \exp\left(\frac{\text{GSI} - 100}{9 - 3D}\right), \tag{11}$$

in terms of the geological strength index GSI and the disturbance factor D. In Figure 3, the influence of GSI and D on the empirical reduction factors, defined by (4), (10) and (11), is depicted.

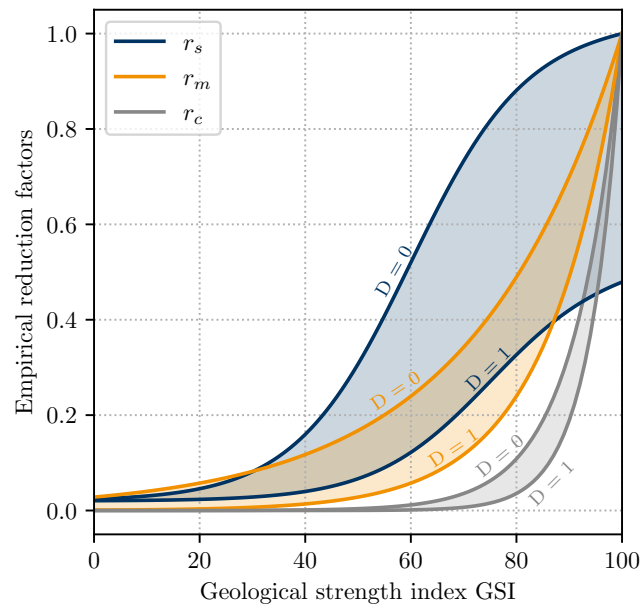


Figure 3. Illustration of the range of the empirical reduction factors r_s , r_m and r_c for the elastic stiffness, the friction parameter and the cohesion parameter, respectively, for $0 \leq D \leq 1$ in terms of the geological strength index GSI.

The shape of the yield function in deviatoric planes is controlled by the Willam–Warnke [49] function $r(\bar{\theta}^*, e)$, defined by the eccentricity parameter e ranging from 0.5 (triangular shape) to 1 (circular shape). The evolution of the yield function (9) is controlled by the stress-like hardening variable $0 \leq q_h(\alpha_p) \leq 1$, depending on the strain-like hardening variable α_p . For $e = 0.5$, the ultimate strength surface $f^*(\bar{\sigma}^*, q_h = 1) = 0$ corresponds to the smooth version of the Hoek–Brown failure criterion, proposed by Menétrey and Willam [11].

For considering the influence of transverse isotropy on the plastic strain tensor $\epsilon^{(p)}$, the non-associated plastic potential function $g^*(\bar{\sigma}^*, q_h(\alpha_p))$ is also formulated in terms of the mapped effective stress tensor, reading as

$$g^*(\bar{\sigma}^*, q_h(\alpha_p)) = \left(\frac{1 - q_h(\alpha_p)}{f_{cu}^{(1)2}} \left(\bar{\sigma}_m^* + \frac{\bar{\rho}^*}{\sqrt{6}} \right)^2 + \sqrt{\frac{3}{2}} \frac{\bar{\rho}^*}{f_{cu}^{(1)}} \right)^2 + \frac{q_h^2(\alpha_p)}{f_{cu}^{(1)}} \left(m_{g1,rm}^* \cdot \bar{\sigma}_m^* + m_{g2,rm}^* \frac{\bar{\rho}^*}{\sqrt{6}} \right). \tag{12}$$

$m_{g1,rm}^* = r_m \cdot m_{g1}^*$ represents a reduced dilatancy parameter, calculated by the dilatancy parameter for intact rock m_{g1}^* , which can be determined from uniaxial compression tests, loaded perpendicular to the planes of isotropy, and triaxial compression tests, loaded in the principal material directions of an intact rock specimen. As described in detail by Unteregger et al. [50], the parameter $m_{g2,rm}^*$ denotes a dependent dilatancy parameter, which can be calculated from $m_{g1,rm}^*$ such that the radial plastic strain rate vanishes in uniaxial tension perpendicular to the planes of isotropy.

For calculating the rate of the plastic strain tensor, the plastic potential function (12) is employed in the non-associated flow rule

$$\dot{\epsilon}^{(p)} = \lambda \mathbb{P} : \frac{\partial g^*(\bar{\sigma}^*, q_h(\alpha_p))}{\partial \bar{\sigma}^*}, \tag{13}$$

with λ denoting the consistency parameter.

The stress-like hardening variable

$$q_h(\alpha_p) = \begin{cases} \frac{f_{cy}^{(1)}}{f_{cu}^{(1)}} + \left(1 - \frac{f_{cy}^{(1)}}{f_{cu}^{(1)}}\right) \alpha_p (\alpha_p^2 - 3\alpha_p + 3) & \alpha_p < 1 \\ 1 & \alpha_p \geq 1 \end{cases}, \tag{14}$$

with the uniaxial compressive yield stress for the loading direction perpendicular to the planes of isotropy $f_{cy}^{(1)}$, is formulated in terms of the strain-like hardening variable α_p , the evolution of which is governed by

$$\dot{\alpha}_p = \lambda \frac{r_s}{x_h^*(\mathbb{H} : \bar{\sigma})} \left(1 + 3 \frac{\bar{\rho}^{*2}}{\bar{\rho}^{*2} + f_{cu}^{(1)2} \cdot 10^{-8}} \cos^2\left(\frac{3\theta^*}{2}\right)\right) \cdot \left\| \mathbb{P} : \frac{\partial g^*(\bar{\sigma}^*, q_h(\alpha_p))}{\partial \bar{\sigma}^*} \right\|. \tag{15}$$

For controlling the ductility of the hardening behavior, the strain-like hardening variable depends on a direction-dependent hardening ductility measure x_h^* , defined as

$$x_h^*(\mathbb{H} : \bar{\sigma}) = \begin{cases} E_h \exp\left(\frac{R_h(\mathbb{H} : \bar{\sigma})}{F_h}\right) + D_h & R_h(\mathbb{H} : \bar{\sigma}) < 0 \\ A_h - (A_h - B_h) \exp\left(\frac{-R_h(\mathbb{H} : \bar{\sigma})}{C_h}\right) & R_h(\mathbb{H} : \bar{\sigma}) \geq 0 \end{cases}, \tag{16}$$

with $R_h(\mathbb{H} : \bar{\sigma}) = -\text{tr}(\mathbb{H} : \bar{\sigma}) / f_{cu}^{(1)} - G_h$ and the hardening parameters A_h, B_h, C_h, D_h and G_h . As described in detail by Mader et al. [32], the dependence of the ductility behavior in the hardening regime on the material orientation can be different from the transversely isotropic variation of the yield surface. Thus, a modified mapping tensor

$$\mathbb{H} = \mathbb{E}^{(1)} + H_h (\mathbb{E}^{(2)} + \mathbb{F} + \mathbb{G}) \tag{17}$$

is defined for controlling the direction dependence of the hardening ductility measure, introducing an additional anisotropy parameter H_h .

2.2. Transversely Isotropic Gradient-Enhanced Damage Behavior

Damage material behavior is initiated when the yield function (9) attains the ultimate strength surface, i.e., at $q_h = 1$. The evolution of the damage variable ω is described by the exponential relation

$$\omega(\alpha_d) = 1 - \exp\left(\frac{-\alpha_d}{\varepsilon_f^{(1)}}\right) \tag{18}$$

as a function of the local damage driving variable α_d . It is controlled by the softening modulus $\varepsilon_f^{(1)}$ for the loading direction perpendicular to the planes of isotropy. The latter can be calibrated by the specific mode I fracture energy $G_{fl}^{(1)}$ for loading perpendicular to the planes of isotropy. The rate equation for the local damage driving variable is given as

$$\dot{\alpha}_d = \begin{cases} 0 & \alpha_p < 1 \\ \frac{\dot{\varepsilon}_{vol}^{(p)}}{x_s(\dot{\varepsilon}^{(p)})} & \alpha_p \geq 1 \end{cases}, \tag{19}$$

with $\dot{\varepsilon}_{vol}^{(p)} = \text{tr}(\dot{\varepsilon}^{(p)})$ and $x_s(\dot{\varepsilon}^{(p)}) = 1 + A_s \left(\dot{\varepsilon}_{\ominus,vol}^{(p)} / \dot{\varepsilon}_{vol}^{(p)}\right)^{B_s}$ denoting the volumetric plastic strain rate and the softening ductility measure, respectively. $\dot{\varepsilon}_{\ominus,vol}^{(p)} = \text{tr}(\langle -\dot{\varepsilon}^{(p)} \rangle)$ represents the compressive part of the volumetric plastic strain rate and A_s and B_s are softening

parameters, which can be calibrated from uniaxial compression tests, loaded perpendicular to the planes of isotropy, and triaxial compression tests, loaded in the principal material directions.

For obtaining mesh-independent results in finite element simulations considering strain softening, the TI-RDP model is regularized by an over-nonlocal implicit gradient enhancement, following Schreter et al. [12]. For this purpose, in (18) α_d is replaced by the over-nonlocal softening variable

$$\hat{\alpha}_d = m \bar{\alpha}_d + (1 - m) \alpha_d. \quad (20)$$

$\bar{\alpha}_d$ represents the nonlocal counterpart of α_d , and m is the weighting parameter. The nonlocal softening variable $\bar{\alpha}_d$ is implicitly determined by the screened Poisson equation

$$\alpha_d = \bar{\alpha}_d - l^2 \nabla^2 \bar{\alpha}_d, \quad (21)$$

with l denoting an internal length scale parameter. The weak form of (21) together with the weak form of the equilibrium equations yields a coupled system of differential equations with the displacements $\mathbf{u}(\mathbf{x})$ and the nonlocal softening variable $\bar{\alpha}_d(\mathbf{x})$ as the primary unknowns. A detailed description of the over-nonlocal implicit gradient enhancement can be found in Schreter et al. [12].

Note that according to (13), the rate of the plastic strain tensor depends on the mapping tensor \mathbb{P} . Hence, the evolution of $\hat{\alpha}_d$ and consequently of the damage variable ω are influenced by the direction-dependent material behavior.

3. Parameter Calibration

In the following, the material parameters of the TI-RDP model are calibrated for *Innsbruck quartz-phyllite* based on experimental results of triaxial compression tests performed by Blümel [51] on specimens sampled from a construction site of the Brenner Base Tunnel. The eccentricity parameter e in (9) cannot be calibrated by triaxial compression tests. It is assumed as $e = 0.51$ as recommended in [50]. In the experimental study, tests with three different confining pressures $\sigma_0 = 12.5$ MPa, 25 MPa and 37.5 MPa and three different directions of axial loading with respect to the inclination of the foliation planes, i.e., $\beta = 0^\circ$, 60° and 90° , were carried out. The cylindrical specimens with a height of 70 mm and a diameter of 35 mm were tested in a displacement controlled manner by monotonically increasing the axial displacement at the top surface of the specimens.

For the parameter calibration, a three-dimensional finite element model of the triaxial compression tests is employed. Compared to commonly used single-element tests for this purpose, by the 3D simulations, also the structural effects, such as non-uniform strain distributions associated with the formation of shear bands, are captured. In Figure 4, the geometry and boundary conditions of the finite element model are illustrated. To reduce the number of degrees of freedom, symmetry is exploited. The specimen is discretized by 20-node quadrilateral finite elements with quadratic shape functions, reduced integration and a characteristic element size of 2.5 mm, resulting in 53,582 degrees of freedom in total. For triggering strain localization, in a small zone at the center of the specimen, elements with slightly reduced values for $f_{cu}^{(1)}$ and $f_{cy}^{(1)}$ by 5% are considered, cf. Figure 4.

The material parameters E_1 , E_2 , ν_{12} , ν_{23} , G_{12} , $f_{cu}^{(1)}$, $f_{cy}^{(1)}$, m_0^* , m_{g1}^* , A_h , B_h , γ , δ and H_h of the TI-RDP model are calibrated such that a best fit with the experimentally determined deviatoric stress–strain curves is obtained from tests with identical values of σ_0 and β . For this purpose, the sum of nonlinear least-squares is minimized by using the *trust-region constrained algorithm* available within the framework of the `scipy.optimize` module [52] of Python. The calibrated material parameters are constrained to positive values, i.e., the lower bounds are set to zero. In addition, $f_{cu}^{(1)}$ is restricted to an upper bound of 200 MPa and $f_{cy}^{(1)} < f_{cu}^{(1)}$ is applied as a linear constraint. This way, a unique local minimum could be found within the prescribed physically meaningful range of the material parameters

for *Innsbruck quartz-phyllite*. The axial strain is taken as the top displacement divided by the initial length of the specimens. The hardening parameters C_h , D_h and G_h , the softening parameters A_s and B_s and the eccentricity parameter e are chosen as recommended by Unteregger et al. [50]. The softening modulus $\varepsilon_f^{(1)}$ perpendicular to the foliation planes and the internal length parameter l are chosen such that a characteristic value of the specific mode I fracture energy $G_f^{(1)}$ for uniaxial tension perpendicular to the foliation planes of 0.15 N/mm, as suggested by Schreter et al. [39], is obtained. The calibrated parameters and the hardening and softening parameters are listed in Table 1.

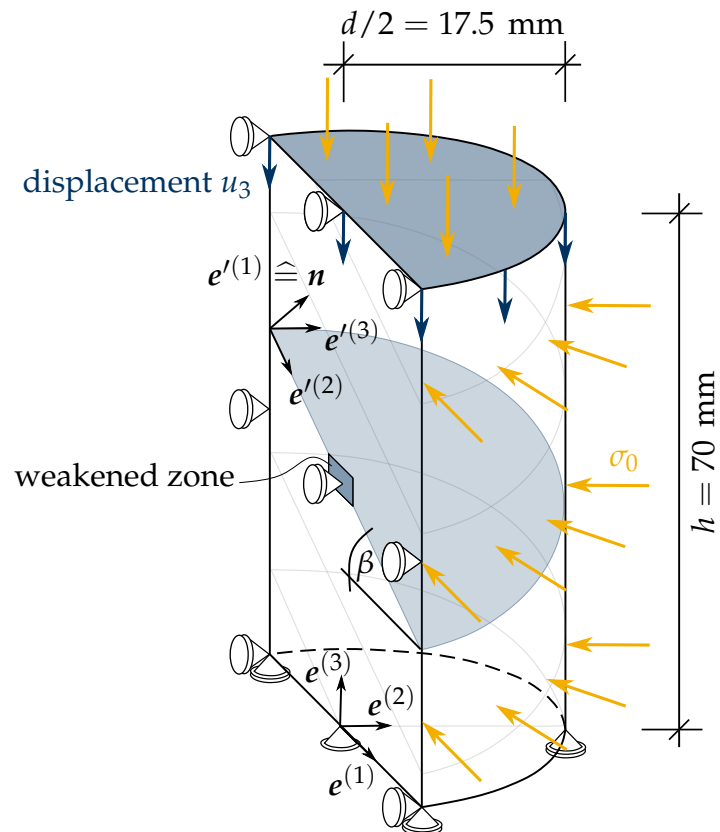


Figure 4. Illustration of the geometry of a specimen together with the orientation of the foliation planes β and the boundary conditions (prescribed top displacement u_3 ; confining pressure σ_0).

Table 1. Material parameters of the TI-RDP model for intact *Innsbruck quartz-phyllite*.

E_1 (MPa)	E_2 (MPa)	ν_{12} (-)	ν_{23} (-)	G_{12} (MPa)	$f_{cu}^{(1)}$ (MPa)	m_0^* (-)	e (-)
45,000	39,000	0.254	0.165	17,000	63.91	19.98	0.51
m_{g1}^* (-)	$f_{cy}^{(1)}$ (MPa)	A_h (-)	B_h (-)	C_h (-)	D_h (-)	G_h (-)	H_h (-)
6.77	25.5	9.5×10^{-3}	1.0×10^{-3}	8.817	1.0×10^{-6}	0.0	1.529
γ (-)	δ (-)	A_s (-)	B_s (-)	$\varepsilon_f^{(1)}$ (-)	l (mm)	GSI (-)	D (-)
1.529	1.201	20	1	3.4×10^{-4}	2.5	100	0

Figure 5 shows the computed maximum deviatoric stress $\sigma_{\text{dev}} = \sigma_{33} - \sigma_0$ in terms of the confining pressure σ_0 and the inclination angle β of the foliation planes, compared to the respective peak values of the experimental data. From Figure 5 follows, for a particular confining pressure, a strong direction dependence of the maximum deviatoric stress.

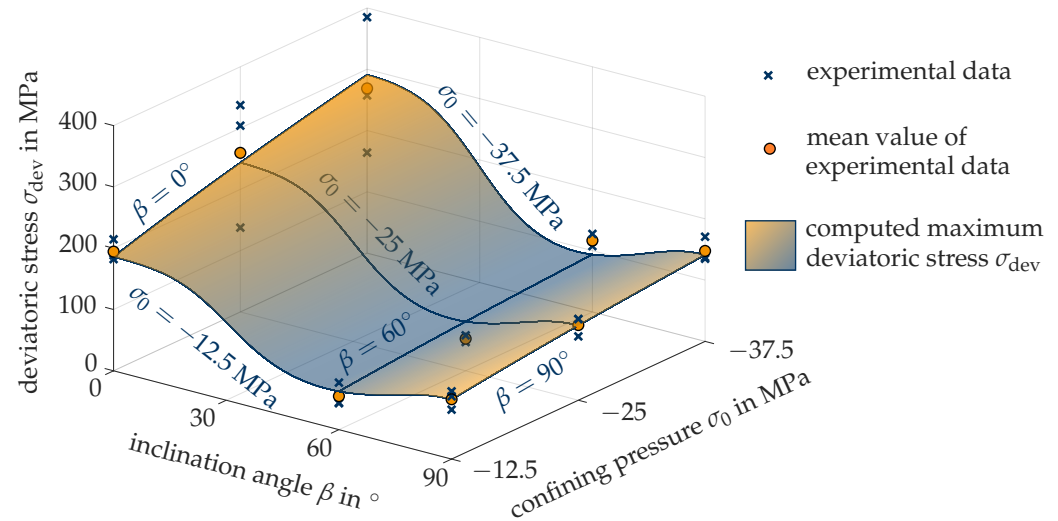


Figure 5. Computed maximum deviatoric stress σ_{dev} in terms of the inclination angle of the foliation planes β and the confining pressure σ_0 together with the experimental data, reprinted with permission from Ref. [51], 2014, Blümel.

Figure 6 shows the computed deviatoric stress-strain curves of the triaxial compression tests together with the corresponding results from the experiments by Blümel [51]. Despite of the large scatter of the experimental results, for the considered confining pressures of $\sigma_0 = 12.5$ MPa, 25 MPa and 37.5 MPa and inclination angles of the foliation planes $\beta = 0^\circ$, 60° and 90° , the numerically predicted strength exhibits good agreement with the corresponding mean values of the experimentally determined strengths.

Furthermore, in the top row of Figure 7, the computed distribution of the displacement magnitude is shown for an advanced stage of the simulation corresponding to a vertical top displacement of $u_3 = -1$ mm, already indicating the predicted failure mode for the confining pressure of 12.5 MPa and the respective inclination angles β . In the bottom row of Figure 7, the corresponding observed failure mechanisms in the experiments are depicted. A comparison of the observed and computed failure modes confirms good agreement for all three inclination angles of the foliation planes.

As noted from Figure 7, the experimentally obtained crack does not necessarily pass through the center of the specimen as predicted by the numerical simulations. This discrepancy in the prediction of the location of the crack is traced back to the location of the introduced artificial imperfection in the numerical model. However, investigations of Desrues and Viggiani [53] concluded that the location of imperfections, e.g., weak elements, does not influence the resulting global stress-strain curves. Thus, it is assumed that the calibration of the material parameters is not affected by the eccentric crack paths.

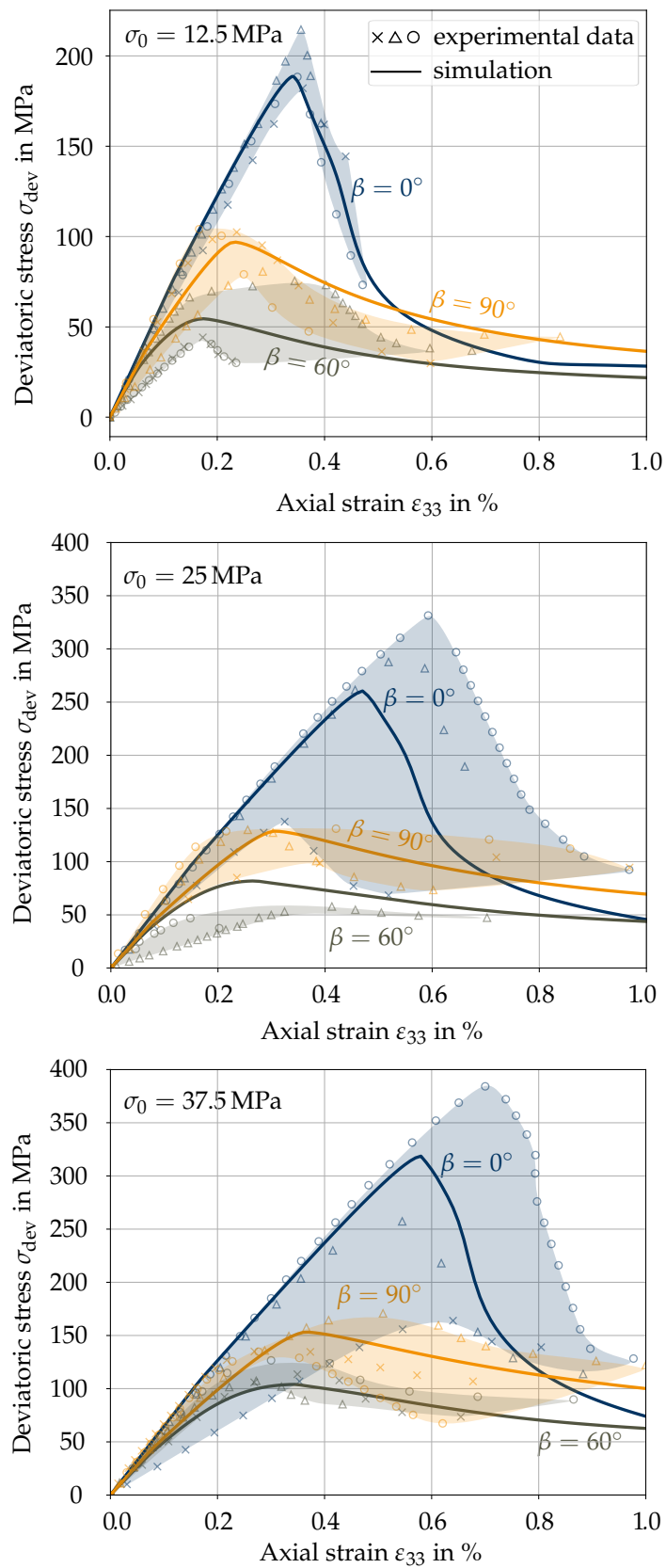


Figure 6. Computed deviatoric stress-strain curves of the triaxial compression tests for confining pressures of $\sigma_0 = 12.5$ MPa (top), 25 MPa (middle) and 37.5 MPa (bottom).

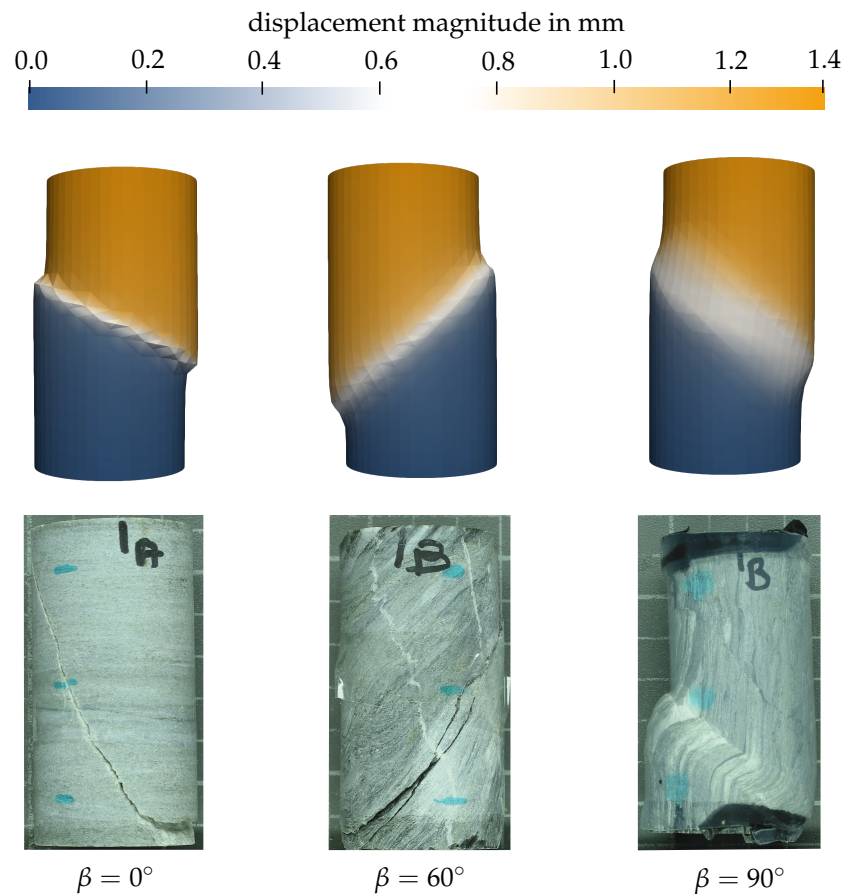


Figure 7. Computed failure modes for $\sigma_0 = 12.5$ MPa for the three inclination angles of the foliation planes $\beta = 0^\circ$, 60° and 90° compared to the experimentally determined failure modes according to Blümel [51] (Images of experiments reprinted with permission from Ref. [51], 2014, Blümel).

4. Numerical Simulation of Tunnel Excavation

The application of the gradient-enhanced transversely isotropic RDP model is demonstrated by predicting the formation of the complex pattern of shear bands due to the excavation of a deep tunnel. To this end, two-dimensional simulations of the excavation of a stretch of the Brenner Base Tunnel, constructed by the drill and blast method, are performed. In a previous publication [12], the respective stretch was already the subject of a mesh study for investigating the capabilities of the gradient-enhanced regularization of the isotropic version of the rock damage-plasticity model ensuring mesh-independent response. Compared to the results of the latter, the impact of different orientations of the principal material directions of foliated rock mass will be demonstrated.

The finite element mesh together with the initial and boundary conditions is illustrated in Figure 8. The tunnel profile is characterized by a circular cross section with a diameter of 8.5 m and an overburden of 950 m at the tunnel axis. To ensure a negligible influence of the boundary conditions (cf. Figure 8 left) on the stress distribution in the vicinity of the tunnel, the considered area of the surrounding rock mass is chosen as $200 \text{ m} \times 200 \text{ m}$.

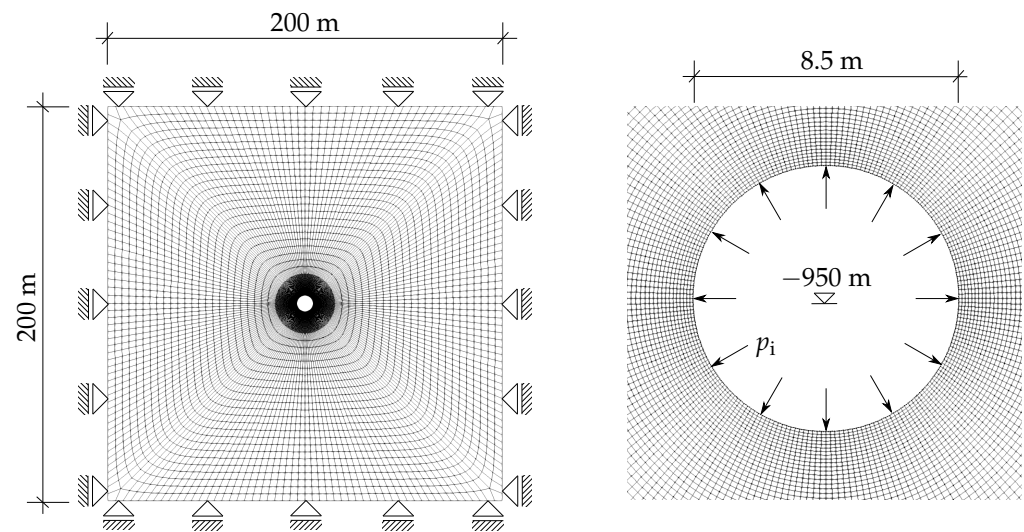


Figure 8. Illustration of the 2D finite element model of the tunnel excavation: full model (left) and detailed view of the FE-mesh in the vicinity of the circular tunnel (right).

The model is discretized by 48,980 8-node finite elements with quadratic shape functions and reduced integration, resulting in 589,508 degrees of freedom. For triggering localized behavior, randomly chosen 20% of the elements in the near field of the tunnel cross section are weakened by reducing the uniaxial compressive strength $f_{cu}^{(1)}$ and the uniaxial yield strength $f_{cy}^{(1)}$ perpendicular to the foliation planes by 5%. For obtaining a high resolution of the localized shear bands in the vicinity of the tunnel, a finer mesh (cf. Figure 8) with a typical element size of ~ 0.05 m is chosen in this region.

Due to the high overburden, a spatially uniform distribution of the geostatic stress state, characterized by the hydrostatic pressure of $p_i^{(0)} = 25.5$ MPa is assumed. It is determined from the density of *Innsbruck quartz-phyllite* of 2739 kg/m³. For the same reason, gravity is not active in the numerical model. For obtaining the most unfavorable excavation conditions, full-face excavation is assumed. At the beginning of the simulation, the initial stress state is represented by applying the hydrostatic pressure as initial stress in the discretized domain and the surface pressure $p_i = p_i^{(0)}$ at the excavation boundary as shown in Figure 8 right. The latter is released continuously for modeling the excavation process in the 2D numerical simulation of tunneling. The excavation is completed upon full release of the surface pressure. Failure of the rock mass in the vicinity of the tunnel is indicated, if full release of the surface pressure is not possible in the numerical simulation.

Since the focus of this contribution is on the influence of directional-dependent behavior of rock mass on the stress redistribution during the excavation process, supporting measures, such as a shotcrete shell or rock anchors, are neglected.

The material parameters for *Innsbruck quartz-phyllite* are adopted from the calibrated parameters for intact rock as listed in Table 1. For considering the effects of present joints and discontinuities in the rock mass, the geological strength index is set to $GSI = 40$ as reported in [12]. In contrast to Table 1, the internal length parameter is increased to $l = 50$ mm in view of the considerably larger dimensions of the tunnel model. Accordingly, the softening modulus in the direction perpendicular to the foliation planes is determined as $\varepsilon_f^{(1)} = 7 \times 10^{-4}$, thus preserving the mode I fracture energy of the triaxial compression tests.

4.1. Influence of the Anisotropy Parameters

For investigating the influence of the transversely isotropic behavior predicted by the TI-RDP model on the mechanical response due to tunnel excavation, a parameter study based on the variation of the two anisotropy parameters γ and δ (7) is performed. γ and δ represent the ratio of the uniaxial compressive strength perpendicular and parallel to the foliation planes and the ratio of the shear strength in the planes of isotropy and

in planes perpendicular to the latter, respectively. A horizontally foliated rock mass ($\beta = 0^\circ$) is considered.

As a benchmark for assessing the influence of the anisotropy parameters γ and δ serves the simulation with the isotropic RDP model. For the latter, the parameters $\gamma = 1$, $\delta = 1$ and the isotropic elastic stiffness tensor in the stress-strain relation (1) with a Young's modulus of $E = E_1 = E_2 = 45,000$ MPa, a Poisson's ratio of $\nu = \nu_{12} = \nu_{23} = 0.254$ and a shear modulus of $G = G_{12} = E/(2(1 + \nu))$ are employed.

Figure 9 shows the distribution of the damage variable ω (left) and the displacement magnitude (right) in the final stage of the simulation before failure, i.e., for a release of the surface pressure of 97.5%. Due to the excavation, for a release of the surface pressure exceeding $\sim 90\%$, the rock mass is subjected to softening, which leads to localization of strains into multiple distinct shear bands, cf. Figure 9 left. In the simulation, strain localization is triggered by the weakened elements, mentioned in Section 4, breaking the otherwise expected axisymmetric behavior. A similar shape of the damage pattern was observed in experiments performed, for example, by Papamichos et al. [54] or Meier et al. [55].

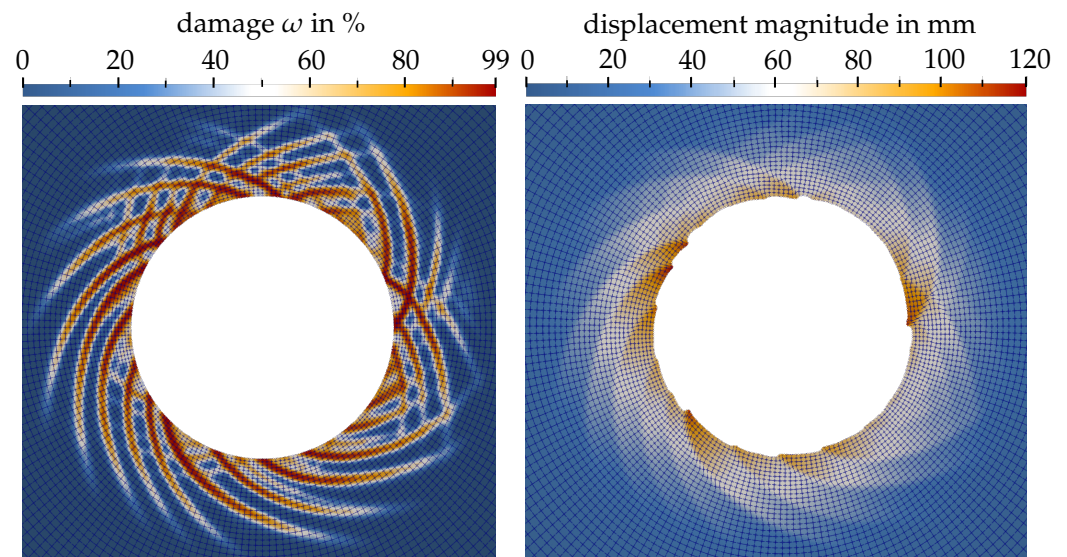


Figure 9. Distribution of the damage variable ω (left) and the displacement magnitude (right) (displacement scale factor 3) in the final stage of the tunnel simulation using the isotropic RDP model.

In Figure 10, the distribution of the damage variable ω (left) and the displacement magnitude (right) is shown for two different values of the anisotropy parameter $\gamma = 1.25$ (top) and $\gamma = 0.75$ (bottom) and a constant value of $\delta = 1$ in the final stage of the simulation before failure, at a release of the surface pressure p_i of 96%. From Figure 10A,B follows that for $\gamma = 1.25$ the highly damaged zones are concentrated around the side walls of the tunnel, where the surface pressure p_i acts in the direction parallel to the foliation planes. This is attributed to the lower uniaxial compressive strength parallel to the foliation planes, $f_{cu}^{(2)}$, compared to the uniaxial compressive strength perpendicular to the foliation planes, $f_{cu}^{(1)}$.

In Figure 10C,D the damage distribution and displacement pattern are shown for $\gamma = 0.75$, resulting in a lower value for $f_{cu}^{(1)}$ compared to $f_{cu}^{(2)}$. Compared to the side walls, this results in a concentration of the highly damaged zones and consequently larger displacements at the top and the bottom of the tunnel cross section. Here the surface pressure at the excavation boundary acts in the direction perpendicular to the foliation planes.

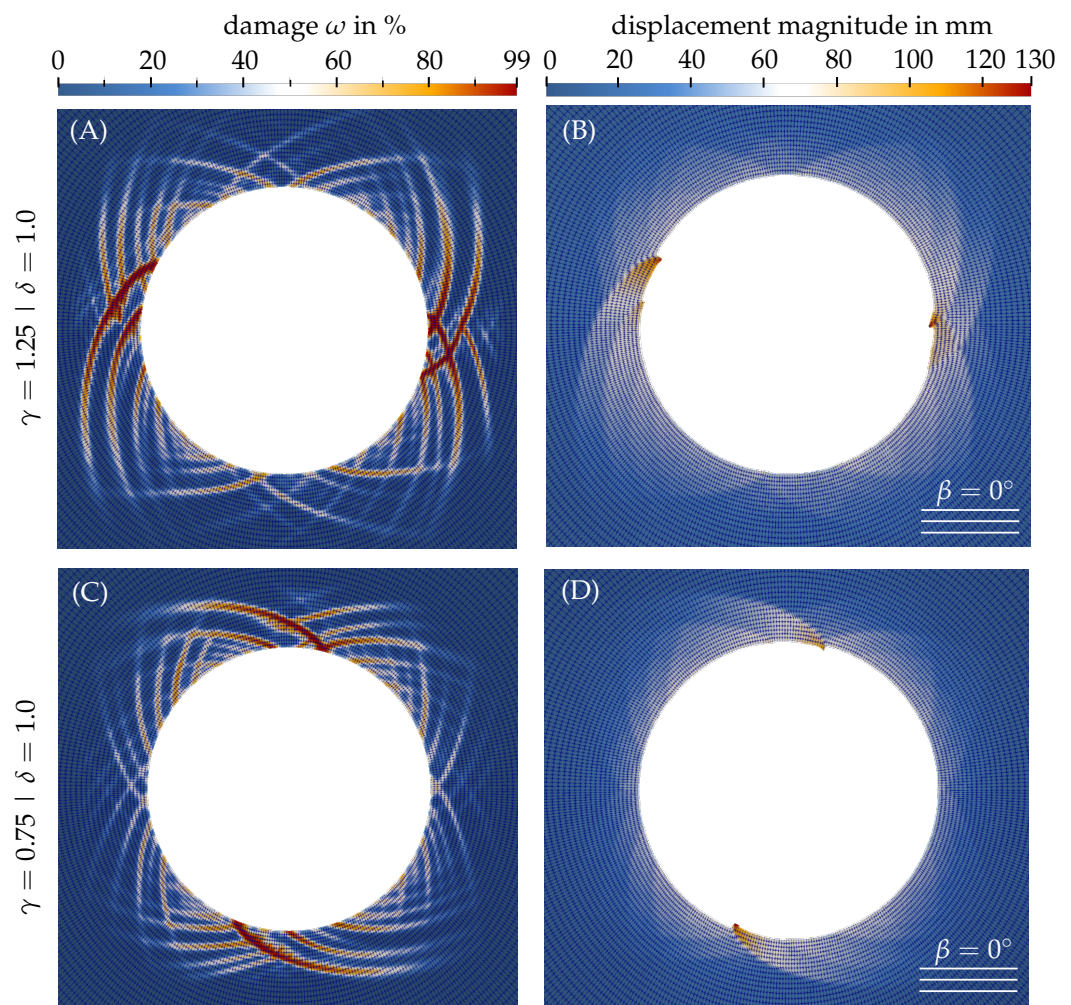


Figure 10. Distribution of the damage variable ω (left—A,C) and the displacement magnitude (right—B,D) (displacement scale factor 3) in the final stage of the tunnel simulation using the **transversely isotropic** RDP model with values of $\gamma = 1.25$ (top—A,B) and 0.75 (bottom—C,D) and a constant value $\delta = 1$.

Figure 11 shows the distribution of the damage variable ω (left) and the displacement magnitude (right) obtained for different values of $\delta = 1.25$ (top) and 0.75 (bottom) and a constant value of $\gamma = 1.0$ in the final stage of the simulation before failure at a release of the surface pressure p_1 of 97.5%. For the considered horizontally foliated rock mass $\beta = 0^\circ$, due to the transversely isotropic linear elastic material behavior, the magnitude of the principal normal stresses has the most unfavorable effect in the horizontal and vertical planes. For this reason, at the top, bottom and sidewalls of the tunnel the damage variable and the displacement magnitude exhibit maximum values. In the present case of a two-dimensional analysis, δ represents a scale factor of the shear strength $f_{sh}^{(12)}$ in planes perpendicular to the foliation planes. Thus, by comparison of the results for $\delta = 0.75$ (cf. Figure 11C,D) and $\delta = 1.25$ (cf. Figure 11A,B), it can be seen that due to the higher shear strength predicted for $\delta = 0.75$ compared to $\delta = 1.25$, the highly damaged zones become smaller and, hence, the displacement magnitude is reduced significantly by a factor of 0.37.

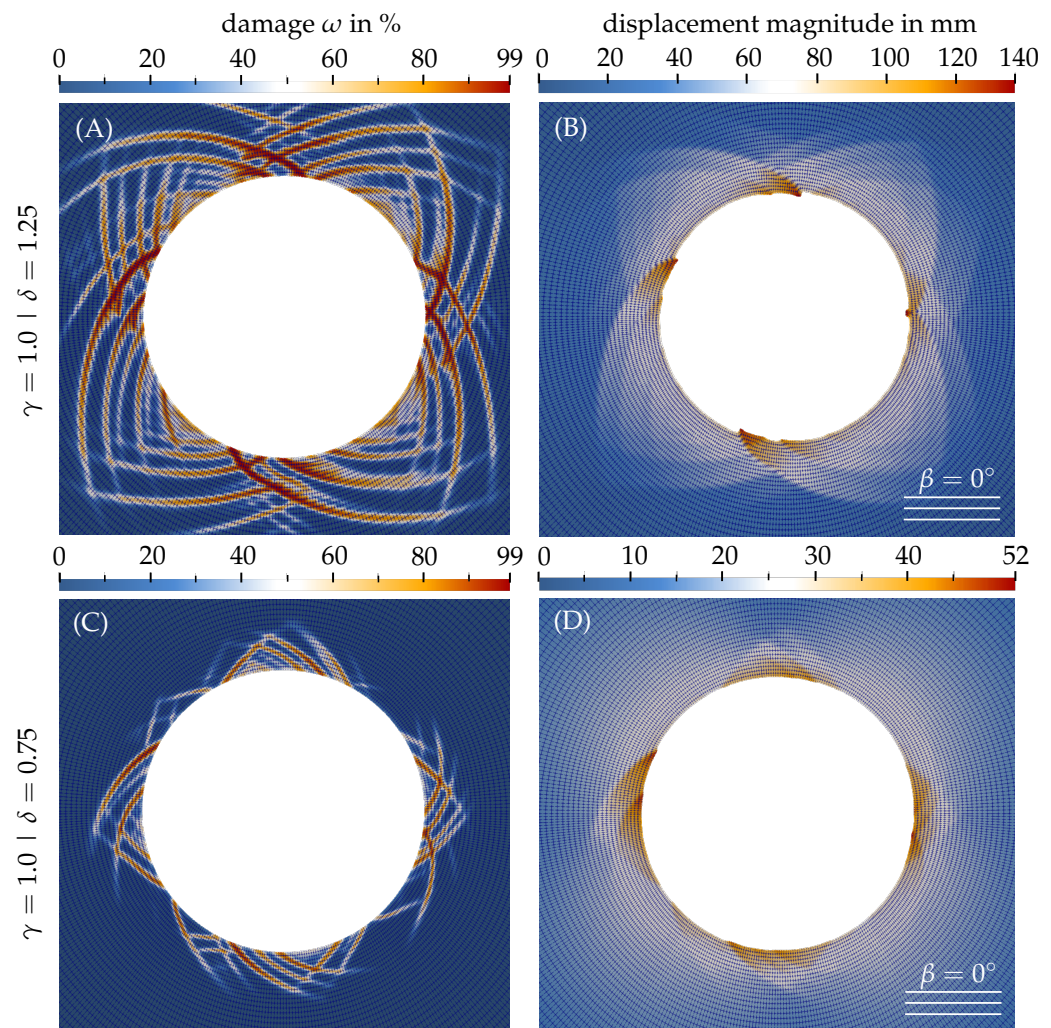


Figure 11. Distribution of the damage variable ω (left—A,C) and the displacement magnitude (right—B,D) (scale factor = 3) in the final stage of the tunnel simulation using the **transversely isotropic** RDP model with values of $\delta = 1.25$ (top—A,B) and 0.75 (bottom—C,D) and a constant value $\gamma = 1$.

By comparing the results obtained by the isotropic RDP model, shown in Figure 9, and by the TI-RDP model, shown in Figures 10 and 11, the influence of the anisotropy parameters can be summarized as follows: For a horizontally layered rock mass, depending on the ratio between the uniaxial compressive strength parallel and perpendicular to the foliation planes, failure at either the side walls or at the tunnel crown and invert is predicted. This is in contrast to the simulations with the isotropic RDP model, where several highly damaged zones are distributed around the tunnel perimeter. Furthermore, it was shown that a smaller shear strength influences the mechanical behavior significantly in the highly damaged zones due to larger shear deformations as well as in zones where the predominant loading direction is inclined to the foliation planes.

4.2. Influence of the Inclination of the Foliation Planes

The influence of the inclination of the foliation planes on the mechanical response of the 2D tunneling simulation is investigated by considering four different values of the inclination angles of the foliation planes $\beta = 0^\circ, 30^\circ, 60^\circ$ and 90° .

In Figure 12, the distribution of the damage variable ω is shown for the four inclination angles β in the final stage of the simulation before failure at a release of the surface pressure p_i of 97.5%. It can be seen that the failure pattern, manifested by the distribution of the highly damaged zones, strongly depends on the inclination angle of the layered rock mass. Considering the mechanical properties of *Innsbruck quartz-phyllite*, cf. Table 1

($\gamma = 1.529$, $\delta = 1.201$, $E_2/E_1 = 0.87$), it can sustain higher loads for loading perpendicular to the foliation planes compared to loading parallel to the foliation planes. Thus, the highly damaged zones are localized where the predominant loading direction, i.e., the direction of the acting surface pressure, is aligned with the foliation planes (cf. Figure 12A–D). Note that for the present axisymmetric tunnel geometry and the hydrostatic initial geostatic stress, the damage patterns for the different inclinations of the foliation planes are not only obtained by a rotation around the tunnel center but are also slightly affected by the randomly distributed weakened zones.

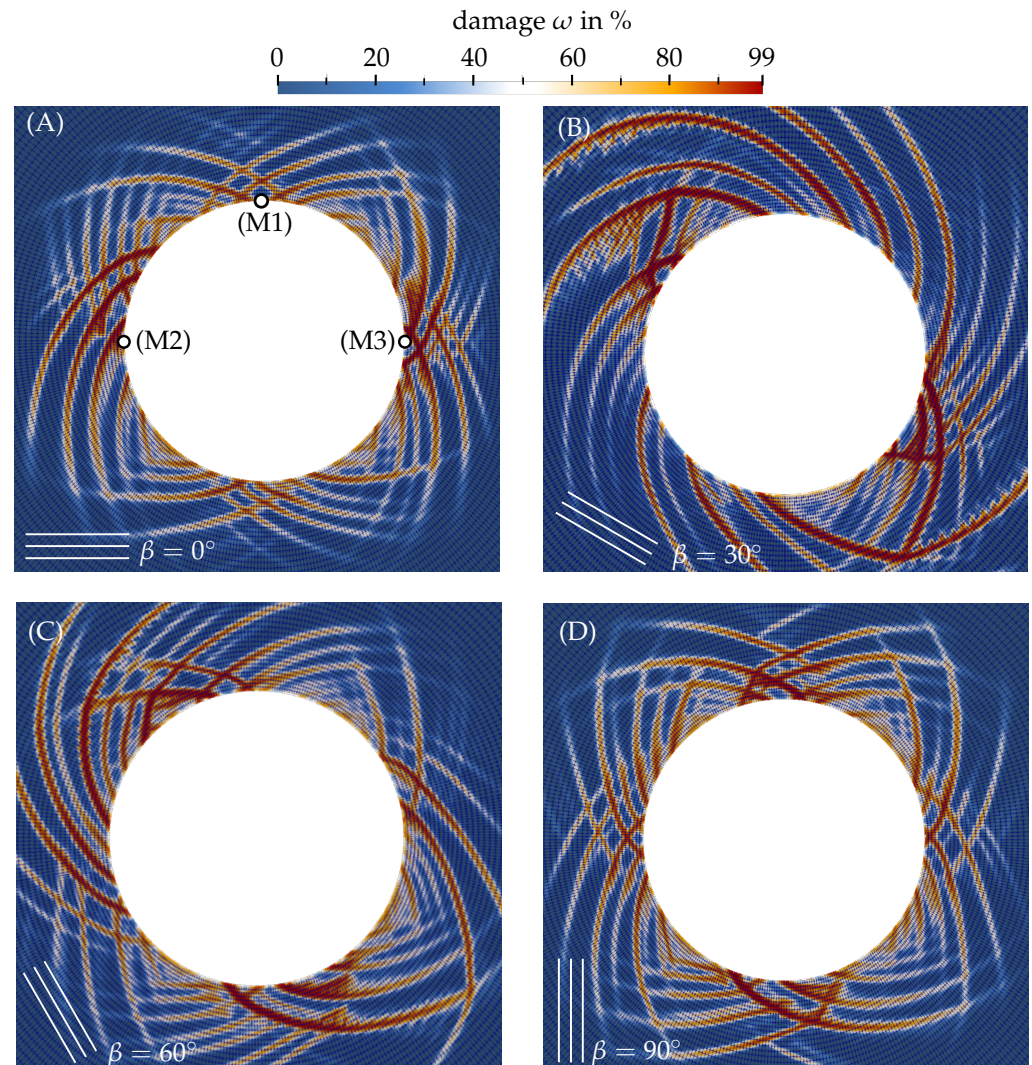


Figure 12. Distribution of the damage variable ω in the final stage of the simulation, determined by the **transversely isotropic** RDP model with the calibrated material parameters of Section 3 for four different inclination angles β of the foliation planes, i.e., $\beta = 0^\circ$ (A), $\beta = 30^\circ$ (B), $\beta = 60^\circ$ (C) and $\beta = 90^\circ$ (D).

In Figure 13, the release of the normalized surface pressure $p_i/p_i^{(0)}$ is depicted in terms of the displacement magnitude for three characteristic points, i.e., top (M1), left (M2) and right side wall (M3) of the tunnel (cf. Figure 12A) and the four inclination angles $\beta = 0^\circ$, 30° , 60° and 90° . In addition, the corresponding results from the simulation using the isotropic RDP model are shown.

Up to a stress release of 90%, i.e., $p_i/p_i^{(0)} = 10\%$, the influence of the inclination of the foliation planes on the displacement magnitude is negligible for the three considered points M1 to M3. However, from the onset of softening behavior, i.e., for a stress release

exceeding 90%, the displacement magnitude varies significantly since the strains localize into narrow zones of the rock mass, leading to the formation of shear bands in the vicinity of the tunnel. Since no securing measures are considered in this study, equilibrium is lost beyond the stress release of approximately 97.5%.

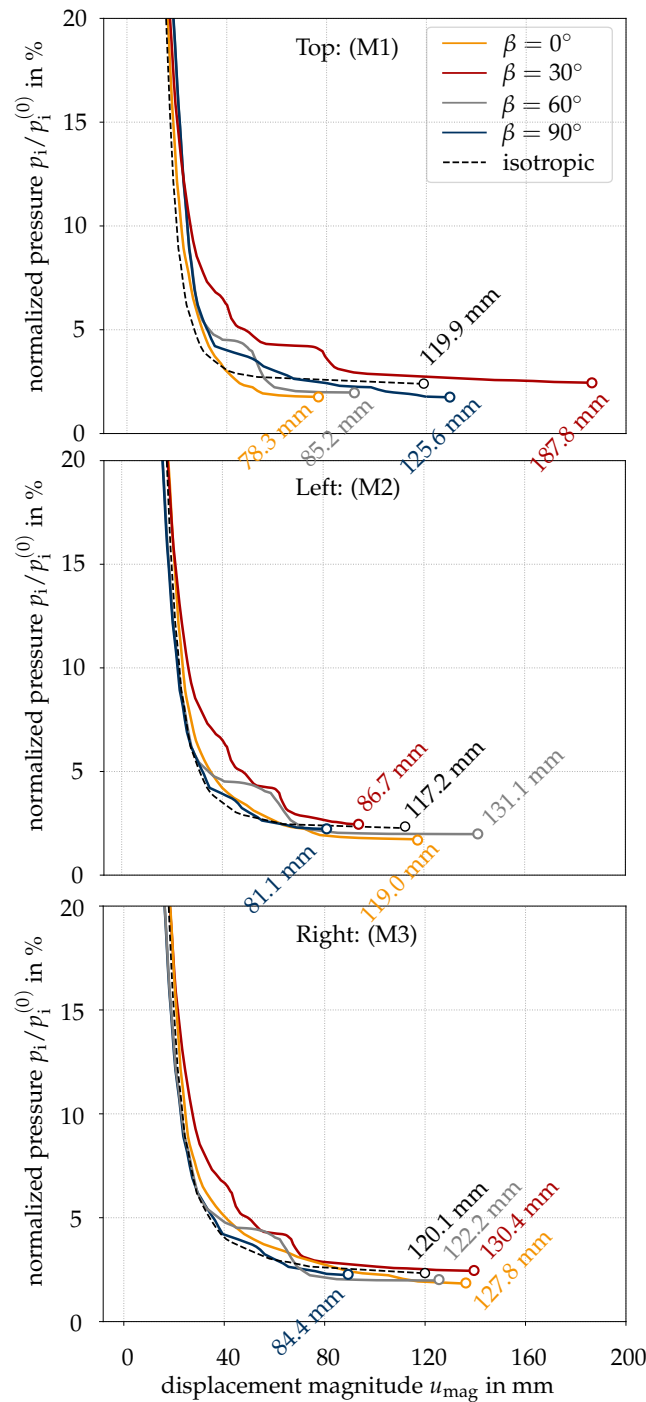


Figure 13. Normalized surface pressure $p_i / p_i^{(0)}$ as a function of the displacement magnitude u_{mag} for three characteristic points, i.e., Top: M1 (top), Left: M2 (middle) and Right: M3 (bottom) and the four inclination angles of the foliation planes $\beta = 0^\circ$ (orange), 30° (red), 60° (grey) and 90° (blue) compared to the isotropic (dashed) simulation.

By employing the **isotropic** RDP model (dashed line), the displacement magnitude in the final stage of the simulation is in the range of 117 to 120 mm at the top and the side

walls of the tunnel cross section (cf. Figure 13 (M1) to (M3)). The slight deviations of the latter are explained by the formation of shear bands due to the randomly distributed weak zones in the near field of the tunnel.

Employing the **transversely isotropic** RDP model, for a horizontally layered rock mass, i.e., $\beta = 0^\circ$, the displacement magnitude at the top (cf. Figure 13 (M1)) is about 2/3 of the respective value predicted at the side walls (cf. Figure 13 (M2) and (M3)). This is attributed to the lower strength in the direction parallel to the foliation planes compared to the perpendicular direction. For a vertically layered rock mass, i.e., $\beta = 90^\circ$, the mechanical response is identical to $\beta = 0^\circ$ apart from a rotation by 90° : the displacement magnitude at the top is by a factor of 1.5 larger than the one on the side walls of the tunnel. For $\beta = 30^\circ$ and 60° , strongly varying values of the maximum displacement magnitude are obtained at the considered points (cf. Figure 13 (M1) to (M3)), underlining the significant influence of the direction dependence. Hence, a distinct asymmetric deformation pattern of the tunnel cross section is obtained.

It is concluded that the direction-dependent material behavior in combination with softening rock mass behavior, accompanied by localization of deformations into narrow zones and the formation of shear bands, has a significant influence on the deformation pattern of the tunnel cross section.

5. Conclusions

This contribution is focused on the influence of direction-dependent and nonlinear material behavior of stratified or foliated rock mass on the mechanical response in deep tunneling. For this purpose, the **transversely isotropic rock damage plasticity** (TI-RDP) model, recently proposed by Mader et al. [32], was used for modeling the combined effects of nonlinear and direction-dependent rock mass behavior in finite element simulations of tunnel advance of a well-monitored stretch of the Brenner Base Tunnel.

The TI-RDP model was formulated by a combination of (i) the isotropic RDP model proposed by Unteregger et al. [9], considering strain hardening, strain softening and the degradation of the material stiffness due to damaging processes and (ii) the approach by Boehler [25] for considering the transversely isotropic material behavior of stratified or foliated rock. For obtaining mesh-insensitive results for the softening behavior, the TI-RDP is regularized by an implicit over-nonlocal gradient-enhancement according to Schreter et al. [12]. For considering discontinuities such as joints or faults, which are typical for rock mass, an extension of the TI-RDP model from stratified or foliated intact rock to rock mass, following the approach by Hoek et al. [6], was presented in this paper.

The material parameters of the TI-RDP model for *Innsbruck quartz-phyllite* were calibrated by means of triaxial compression tests. To this end, 3D finite element simulations of intact rock specimens were conducted for different angles of the foliation planes with respect to the loading direction and different confining pressures. The parameters were identified by means of the experimentally determined load-displacement curves by Blümel [51]. It was shown that in spite of the varying loading angles and confining pressures, good agreement of both the load-displacement curves and the failure modes was obtained.

Next, a 2D finite element model considering tunnel excavation in *Innsbruck quartz-phyllite* was set up for a stretch of the Brenner Base Tunnel. Studies on the influence of the anisotropy parameters of the TI-RDP model in a horizontally layered rock mass and the influence of the orientation of the foliation planes on the mechanical response of the rock mass were presented. The results of the latter were compared to the results predicted by the isotropic RDP model. It was demonstrated that the ratio between the uniaxial compressive strength perpendicular and parallel to the foliation planes significantly influences the location of the highly damaged zones. However, it has only a little effect on the maximum displacement magnitude for a horizontally layered rock mass. In the 2D simulations, the ratio between the shear strength in the plane of isotropy and the shear strength in planes perpendicular to the latter had no impact on the location of the highly damaged zones and thus did not influence the direction-dependent behavior. However, it significantly influenced the predicted displacement magnitude along the tunnel perimeter.

For determining the influence of the orientation of the foliation planes on the mechanical response of the rock mass, 2D finite element simulations of tunnel excavation were performed for different angles of the foliation planes $\beta = 0^\circ, 30^\circ, 60^\circ$ and 90° . As the formation pattern of shear bands depends on the orientation of the foliation planes, a strongly direction-dependent deformation pattern of the tunnel cross section was obtained. Thus, consideration of the direction-dependent material behavior, particularly with nonlinear stress–strain relations, including strain hardening and softening, is indispensable for predicting the mechanical response of stratified or foliated rock mass in numerical simulations of tunnel excavation.

Author Contributions: Conceptualization of the paper by T.M., M.S. and G.H.; Extension of the constitutive model for direction-dependent behavior, calibration of the model and performance of the simulations by T.M.; Implementation of the numerical framework and evaluation of the results by T.M. and M.S.; Writing, review and editing of the paper by T.M., M.S. and G.H.; Supervision, G.H. All authors have read and agreed to the published version of the manuscript.

Funding: This research was partially funded by the Tyrolean Science Fund with the grant number F.18712.

Data Availability Statement: The data that support the findings of this study are available from the corresponding author upon reasonable request.

Conflicts of Interest: The authors declare no conflict of interest.

Appendix A

Table A1. List of symbols.

General notations			
a'		quantity a with respect to the local coordinate system	
a^*		quantity a with respect to the fictitious isotropic configuration	
\dot{a}		rate of a quantity a	
$a^{(1)} a_1$		quantity a in direction perpendicular to the planes of isotropy	
$a^{(2)} a_2$		quantity a in direction parallel to the planes of isotropy	
$a^{(12)} a_{12}$		quantity a in planes perpendicular to the planes of isotropy	
$a^{(23)} a_{23}$		quantity a in planes of isotropy	
a_{rm}		quantity a of rock mass	
$a^{(0)}$		initial state of a quantity a	
Scalar quantities			
σ_m	Pa	mean stress	m_{g2} - dependent dilatancy parameter
ρ	Pa	deviatoric radius	$\dot{\lambda}$ - consistency parameter
θ	o	lode angle	$\gamma \delta H_h$ - anisotropy parameters
$\varepsilon_{vol}^{(p)}$	-	volumetric plastic strain	q_h - stress-like hardening variable
$\varepsilon_{\ominus,vol}^{(p)}$	-	compressive part of $\varepsilon_{vol}^{(p)}$	α_p - strain-like hardening variable
ω	-	damage variable	$A_h - G_h$ - hardening parameters
E	Pa	Young's modulus	$A_s B_s$ - softening parameters
ν	-	Poisson's ratio	α_d - local softening variable
G	Pa	shear modulus	$\bar{\alpha}_d$ - nonlocal softening variable
GSI	-	geological strength index	$\hat{\alpha}_d$ - over-nonlocal softening variable

Table A1. Cont.

D	-	disturbance factor	m	-	weighting parameter
r_s	-	empirical stiffness reduction factor	l	m	internal length scale
r_m	-	empirical friction reduction factor	G_{fl}	N/m	mode I fracture energy
r_c	-	empirical cohesion reduction factor	ε_f	-	softening modulus
f_{cu}	Pa	uniaxial compressive strength	σ_0	Pa	confining pressure
f_{cy}	Pa	uniaxial compressive yield stress	σ_{dev}	Pa	deviatoric stress
f_{sh}	Pa	shear strength	β	°	inclination angle
e	-	eccentricity parameter	u_3	m	displacement component in x_3 -direction
m_0	-	friction parameter	p_i	Pa	surface pressure
m_{g1}	-	independent dilatancy parameter			
Vectors					
n	-	unit normal vector of the planes of isotropy			
e	-	unit base vectors			
Second-order tensors					
σ	Pa	Cauchy stress tensor	\mathbf{a}	-	orthogonal transformation matrix
$\bar{\sigma}$	Pa	effective Cauchy stress tensor	ϕ	-	microstructure tensor
ε	-	linearized strain tensor	χ	-	orthogonal tensor to ϕ
$\varepsilon^{(p)}$	-	plastic part of the linearized strain tensor			
Fourth-order tensors					
$\mathbb{C}^{(ti)}$	Pa	transversely isotropic elastic stiffness tensor			
\mathbb{P}	-	mapping tensor			
\mathbb{H}	-	modified mapping tensor			
$\mathbb{E} \mathbb{F} \mathbb{G}$	-	sub-tensors of \mathbb{P} and \mathbb{H}			

References

- Lisjak, A.; Grasselli, G. A review of discrete modeling techniques for fracturing processes in discontinuous rock masses. *J. Rock Mech. Geotech. Eng.* **2014**, *6*, 301–314. <https://doi.org/10.1016/j.jrmge.2013.12.007>.
- Jing, L.; Hudson, J. Numerical methods in rock mechanics. *Int. J. Rock Mech. Min. Sci.* **2002**, *39*, 409–427. [https://doi.org/10.1016/S1365-1609\(02\)00065-5](https://doi.org/10.1016/S1365-1609(02)00065-5).
- Jing, L. A review of techniques, advances and outstanding issues in numerical modelling for rock mechanics and rock engineering. *Int. J. Rock Mech. Min. Sci.* **2003**, *40*, 283–353. [https://doi.org/10.1016/S1365-1609\(03\)00013-3](https://doi.org/10.1016/S1365-1609(03)00013-3).
- Barton, N. Shear strength criteria for rock, rock joints, rockfill and rock masses: Problems and some solutions. *J. Rock Mech. Geotech. Eng.* **2013**, *5*, 249–261.
- Wittke, W. *Rock Mechanics Based on an Anisotropic Jointed Rock Model (AJRM)*; John Wiley & Sons: Hoboken, NJ, USA, 2014.
- Hoek, E.; Diederichs, M.S. Empirical estimation of rock mass modulus. *Int. J. Rock Mech. Min. Sci.* **2006**, *43*, 203–215.
- Hoek, E.; Carranza-Torres, C.; Corkum, B. Hoek-Brown failure criterion—2002 ed. In Proceedings of the 5th North American Rock Mechanics Symposium and the 17th Tunnelling Association of Canada, Toronto, ON, Canada, 7–10 July; Hammah, R., Ed.; University of Toronto Press, Toronto, ON, Canada, 2002; pp. 267–273.
- Hoek, E.; Brown, E.T. Empirical strength criterion for rock masses. *J. Geotech. Eng. Div. Proc. Am. Soc. Civ. Eng.* **1980**, *106*, 1013–1035.
- Unteregger, D.; Fuchs, B.; Hofstetter, G. A damage plasticity model for different types of intact rock. *Int. J. Rock Mech. Min. Sci.* **2015**, *80*, 402–411. <https://doi.org/10.1016/j.ijrmms.2015.09.012>.
- Grassl, P.; Jirásek, M. Damage-plastic model for concrete failure. *Int. J. Solids Struct.* **2006**, *43*, 7166–7196. <https://doi.org/10.1016/j.ijsolstr.2006.06.032>.

11. Men etrey, P.; Willam, K. Triaxial failure criterion for concrete and its generalization. *Struct. J.* **1995**, *92*, 311–318.
12. Schreter, M.; Neuner, M.; Hofstetter, G. Evaluation of the implicit gradient-enhanced regularization of a damage-plasticity rock model. *Appl. Sci.* **2018**, *8*, 1004. <https://doi.org/10.3390/app8061004>.
13. Hill, R. A theory of the yielding and plastic flow of anisotropic metals. *Proc. R. Soc. London. Ser. A Math. Phys. Sci.* **1948**, *193*, 281–297. <https://doi.org/10.1098/rspa.1948.0045>.
14. Pariseau, W.G. Plasticity theory for anisotropic rocks and soil. In Proceedings of the 10th U.S. Symposium on Rock Mechanics (USRMS), Austin, TX, USA, 20–22 May 1968; pp. 267–295.
15. Tsai, S.W.; Wu, E.M. A general theory of strength for anisotropic materials. *J. Compos. Mater.* **1971**, *5*, 58–80. <https://doi.org/10.1177/002199837100500106>.
16. Jaeger, J. Shear failure of anisotropic rocks. *Geol. Mag.* **1960**, *97*, 65–72.
17. Goodman, R.E. *Research on Rock Bolt Reinforcement and Integral Lined Tunnels*; Technical Report; No. OMAHA-TR-3.; Corps of Engineers: Omaha, NE, USA, 1967.
18. Ismael, M.; Konietzky, H. Integration of elastic stiffness anisotropy into ubiquitous joint model. *Procedia Eng.* **2017**, *191*, 1032–1039. <https://doi.org/10.1016/j.proeng.2017.05.276>.
19. Ismael, M.; Konietzky, H.; Herbst, M. A new continuum-based constitutive model for the simulation of the inherent anisotropy of Opalinus clay. *Tunn. Undergr. Space Technol.* **2019**, *93*, 103106. <https://doi.org/10.1016/j.tust.2019.103106>.
20. Pietruszczak, S.; Mroz, Z. Formulation of anisotropic failure criteria incorporating a microstructure tensor. *Comput. Geotech.* **2000**, *26*, 105–112. [https://doi.org/10.1016/S0266-352X\(99\)00034-8](https://doi.org/10.1016/S0266-352X(99)00034-8).
21. Gao, Z.; Zhao, J.; Yao, Y. A generalized anisotropic failure criterion for geomaterials. *Int. J. Solids Struct.* **2010**, *47*, 3166–3185. doi:10.1016/j.ijsolstr.2010.07.016.
22. Chen, L.; Shao, J.F.; Huang, H. Coupled elastoplastic damage modeling of anisotropic rocks. *Comput. Geotech.* **2010**, *37*, 187–194.
23. Chen, L.; Shao, J.; Zhu, Q.Z.; Duveau, G. Induced anisotropic damage and plasticity in initially anisotropic sedimentary rocks. *Int. J. Rock Mech. Min. Sci.* **2012**, *51*, 13–23.
24. Parisio, F.; Vilarrasa, V.; Laloui, L. Hydro-mechanical modeling of tunnel excavation in anisotropic shale with coupled damage-plasticity and micro-dilatant regularization. *Rock Mech. Rock Eng.* **2018**, *51*, 3819–3833.
25. Boehler, J. Equilibre limite des sols anisotropes. *J. Mec.* **1970**, *9*, 5–33.
26. Boehler, J.; Sawczuk, A. On yielding of oriented solids. *Acta Mech.* **1977**, *27*, 185–204. <https://doi.org/10.1007/BF01180085>.
27. Crook, A.J.; Yu, J.G.; Willson, S.M. Development of an orthotropic 3D elastoplastic material model for shale. In Proceedings of the SPE/ISRM Rock Mechanics Conference, Irving, TX, USA, 20–23 October 2002; p. 78238. <https://doi.org/10.2118/78238-MS>.
28. Semnani, S.J.; White, J.A.; Borja, R.I. Thermoplasticity and strain localization in transversely isotropic materials based on anisotropic critical state plasticity. *Int. J. Numer. Anal. Methods Geomech.* **2016**, *40*, 2423–2449. <https://doi.org/10.1002/nag.2536>.
29. Bryant, E.C.; Sun, W. A micromorphically regularized Cam-clay model for capturing size-dependent anisotropy of geomaterials. *Comput. Methods Appl. Mech. Eng.* **2019**, *354*, 56–95.
30. Zhao, Y.; Semnani, S.J.; Yin, Q.; Borja, R.I. On the strength of transversely isotropic rocks. *Int. J. Numer. Anal. Methods Geomech.* **2018**, *42*, 1917–1934.
31. Zhao, Y.; Borja, R.I. A double-yield-surface plasticity theory for transversely isotropic rocks. *Acta Geotech.* **2022**, 1–21. <https://doi.org/10.1007/s11440-022-01605-6>.
32. Mader, T.; Schreter, M.; Hofstetter, G. A gradient enhanced transversely isotropic damage plasticity model for rock—Formulation and comparison of different approaches. *Int. J. Numer. Anal. Methods Geomech.* **2022**, *46*, 933–960. <https://doi.org/10.1002/nag.3327>.
33. Vardoulakis, I.; Sulem, J.; Guenot, A. Borehole instabilities as bifurcation phenomena. *Int. J. Rock Mech. Min. Sci. Geomech. Abstr.* **1988**, *25*, 159–170.
34. Crook, T.; Willson, S.; Yu, J.G.; Owen, R. Computational modelling of the localized deformation associated with borehole breakout in quasi-brittle materials. *J. Pet. Sci. Eng.* **2003**, *38*, 177–186.
35. Zervos, A.; Papanastasiou, P.; Cook, J. Elastoplastic finite element analysis of inclined wellbores. In *SPE/ISRM Rock Mechanics in Petroleum Engineering*; OnePetro: Richardson, TX, USA, 1998.
36. Alsahly, A.; Stascheit, J.; Meschke, G. Advanced finite element modeling of excavation and advancement processes in mechanized tunneling. *Adv. Eng. Softw.* **2016**, *100*, 198–214.
37. Zhao, K.; Bonini, M.; Debernardi, D.; Janutolo, M.; Barla, G.; Chen, G. Computational modelling of the mechanised excavation of deep tunnels in weak rock. *Comput. Geotech.* **2015**, *66*, 158–171.
38. Sahara, D.P.; Schoenball, M.; Gerolymatou, E.; Kohl, T. Analysis of borehole breakout development using continuum damage mechanics. *Int. J. Rock Mech. Min. Sci.* **2017**, *97*, 134–143.
39. Schreter, M.; Neuner, M.; Unteregger, D.; Hofstetter, G. On the importance of advanced constitutive models in finite element simulations of deep tunnel advance. *Tunn. Undergr. Space Technol.* **2018**, *80*, 103–113. <https://doi.org/10.1016/j.tust.2018.06.008>.
40. Wang, S.; Sloan, S.; Tang, C.; Zhu, W. Numerical simulation of the failure mechanism of circular tunnels in transversely isotropic rock masses. *Tunn. Undergr. Space Technol.* **2012**, *32*, 231–244.
41. Schuller, H.; Schweiger, H. Application of a multilaminar model to simulation of shear band formation in NATM-tunnelling. *Comput. Geotech.* **2002**, *29*, 501–524.

42. Pardoën, B.; Seyedi, D.; Collin, F. Shear banding modelling in cross-anisotropic rocks. *Int. J. Solids Struct.* **2015**, *72*, 63–87. <https://doi.org/10.1016/j.ijsolstr.2015.07.012>.
43. Foderà, G.M.; Voza, A.; Barovero, G.; Tinti, F.; Boldini, D. Factors influencing overbreak volumes in drill-and-blast tunnel excavation. A statistical analysis applied to the case study of the brenner base tunnel—BBT. *Tunn. Undergr. Space Technol.* **2020**, *105*, 103475. <https://doi.org/10.1016/j.tust.2020.103475>.
44. Bistacchi, A.; Massironi, M.; Dal Piaz, G.V.; Dal Piaz, G.; Monopoli, B.; Schiavo, A.; Toffolon, G. 3D fold and fault reconstruction with an uncertainty model: An example from an alpine tunnel case study. *Comput. Geosci.* **2008**, *34*, 351–372. <https://doi.org/10.1016/j.cageo.2007.04.002>.
45. Cordes, T.; Schreter, M.; Schneider-Muntau, B.; Neuner, M.; Bergmeister, K.; Hofstetter, G. On the prediction of the longitudinal displacement profile of a stretch of the brenner base tunnel—Analytical, experimental and numerical approaches. In Proceedings of the Underground Construction, Prague, Czech Republic, 3–5 June 2019.
46. Borja, R.I.; Yin, Q.; Zhao, Y. Cam-Clay plasticity. Part IX: On the anisotropy, heterogeneity, and viscoplasticity of shale. *Comput. Methods Appl. Mech. Eng.* **2020**, *360*, 112695.
47. Bryant, E.C. Capturing Evolving Size-Dependent Anisotropy from Brittle Fracture to Plasticity for Geological Materials. Ph.D. Thesis, Columbia University, New York, NY, USA, 2020.
48. Walpole, L. Fourth-rank tensors of the thirty-two crystal classes: multiplication tables. *Proc. R. Soc. Lond. Math. Phys. Sci.* **1984**, *391*, 149–179.
49. Willam, K.; Warnke, E. Constitutive model for the triaxial behaviour of concrete. *Concr. Struct. Subj. Triaxial Stress. IABSE* **1974**, *9*, 1–30.
50. Unteregger, D.; Hofstetter, G.; Haltmeier, M.; Ostermann, A. Parameter identification for an advanced material model for intact rock. In Proceedings of the 8th European Conference on Numerical Methods in Geotechnical Engineering (NUMGE 2014), Delft, The Netherlands, 18–20 June 2014; Hicks, M.A., Brinkgreve, R.B., Rohe, A., Eds.; CRC Press: Boca Raton, FL, USA, 2014; pp. 215–220.
51. Blümel, M. *Prüfprotokolle Laborversuche Druckversuche Anfahrstutzen Ahrntal*; Technical Report; Institut für Felsmechanik und Tunnelbau TU Graz: Graz, Austria, 2014.
52. Jones, E.; Oliphant, T.; Peterson, P. SciPy: Open Source Scientific Tools for Python. Available online: <https://github.com/scipy/scipy> (accessed on 20 August 2022).
53. Desrues, J.; Viggiani, G. Strain localization in sand: An overview of the experimental results obtained in Grenoble using stereophotogrammetry. *Int. J. Numer. Anal. Methods Geomech.* **2004**, *28*, 279–321. <https://doi.org/10.1002/nag.338>.
54. Papamichos, E.; Liolios, P.; Van den Hoek, P. Breakout stability experiments and analysis. In Proceedings of the Gulf Rocks 2004, the 6th North America Rock Mechanics Symposium (NARMS), Houston, TX, USA, 5–10 June 2004; OnePetro: Richardson, TX, USA, 2004.
55. Meier, T.; Rybacki, E.; Reinicke, A.; Dresen, G. Influence of borehole diameter on the formation of borehole breakouts in black shale. *Int. J. Rock Mech. Min. Sci.* **2013**, *62*, 74–85.